MDPI

Article

A HYBRID CONTINUUM-PARTICLE APPROACH FOR FLUID-STRUCTURE INTERACTION SIMULATION OF RED BLOOD CELLS IN FLUID FLOWS

Lahcen Akerkouch [1] and Trung Bao Le [1,2,3]* 0000-0002-4692-5469

[1] Department of Civil and Environmental Engineering, North Dakota State University, CIE 201, 1410 North 14th Avenue, Fargo, ND 58105-5285, United States
[2] NDSU-UND Biomedical Engineering Program, United States
[3] Center for Cellular Biointerfaces in Science and Engineering, United States
* Correspondence: Trung Bao Le (trung.le@ndsu.edu); Tel.: (+01-701-231-6369 (T.L.)

Citation: Akerkouch, L.; Le, T A hybrid continuum-particle based approach for vesicles. *Fluids* **2021**, *1*, 0. https://dx.doi.org/10.3390/fluids1010000

Received:
Accepted:
Published:

Abstract: Transport of cells in fluid flow plays a critical role in many physiological processes of human body. Recent developments of *in vitro* techniques have enabled the understanding of cellular dynamics in laboratory conditions. However, it is challenging to obtain precise characteristics of cellular dynamics using experimental method alone, especially under *in vivo* conditions. This challenge motivates new developments of computational methods to provide complementary data that experimental techniques are not able to provide. Since there exists a large disparity in spatial and temporal scales in this problem, which requires a large number of cells to be simulated, it is highly desirable to develop an efficient numerical method for the interaction of cells and fluid flows. In this work, a new Fluid-Structure Interaction formulation is proposed based on the use of hybrid continuum-particle approach, which can resolve local dynamics of cells while providing large-scale flow patterns in the vascular vessel. Here, the Dissipative Particle Dynamics (DPD) model for the cellular membrane is used in conjunction with the Immersed Boundary Method (IBM) for the fluid plasma. Our results show that the new formulation is highly efficient in computing the deformation of cells within fluid flow while satisfying the incompressibility constraints of the fluid. We demonstrate that it is possible to couple the DPD with the IBM to simulate the complex dynamics of RBC such as parachuting. Our key observation is that the proposed coupling enables the simulation of RBC dynamics in realistic arterioles while ensuring the incompressibility constraint for the fluid plasma. Therefore, the proposed method allows an accurate estimation of fluid shear stresses on the surface of the simulated RBC. Our results suggest that this hybrid methodology can be extended for a variety of cells in physiological conditions.

Keywords: continuum-particle approach; cells; fluid-structure interaction

1. Introduction

Dynamics of biological cells in fluid flows is important in many areas of bio-engineering [1]. Transport of cells in human body is the main mechanism to sustain life as it provides oxygen, nutrient, and defensive mechanism to fence off infection. Human cells are comprised of many compartments such as bi-lipid membrane, cytoplasm, nucleus, and others [2]. However, special cells such as the Red Blood Cell (RBC), White Blood Cell (WBC), platelet, and contain mostly of a thin membrane and the cytosol fluid [3]. RBC, WBC, and platelet [4] are the main components of human blood. Therefore, understanding their dynamics could lead to new innovations in many engineering areas such as biomedical devices [5,6], cancer biology [7,8], or drug delivery [9]. From a mechanical standpoint, these special cells (or capsules) are deformable bodies, which are immersed in a flowing fluid. Investigating the dynamics of these cells can be useful for many engineering applications such as detection of malaria infection [10], cell sorting/separation[11], drug delivery [12], and design of devices for blood fractionation [13]. Modeling the dynamics of these special cells in fluid flow is the focus of the current work.

While many aspects of cellular flows can be examined by $in-vitro$ experiment [14] in well-controlled conditions, it is challenging to replicate all physiological conditions in the laboratory. In the last decade, numerical simulations have shown their promises [15] in investigating transport of cells in realistic anatomy of vascular systems [2]. The growth of computing power has enabled the simulation of whole blood, which consists of RBC, WBC, and platelet interacting with each other [16]. The central challenge here is the multi-way interactions of these capsules with the fluid flow and with each other. In addition, the complex anatomy of the vascular system is a great challenge for computational methods to deal with [17] since cells migrate along the bifurcations without a predetermined pattern. Here, numerical methods must be able to resolve the local dynamics of cells as well as providing sufficient details of large scale flows in the vascular vessels. This task motivates a variety of approaches as listed below.

In a single cell, molecular dynamics (MD) [18,19] simulation is the method of choice for calculating cellular membrane dynamics since it can provide a good estimation of lipid bilayer dynamics. However, MD requires a large number of particles (few millions) to mimic the behavior of the membrane [19–21]. This approach is thus not appropriate for a large-scale simulation of multiple cells.

Continuum approach such as the Finite Element Method [16,17,22,23] and boundary integral methods [24–26] have been used to describe dynamics of RBC membrane. These continuum approaches require solving the non-linear systems of equations to calculate the finite deformation of the cell membrane. Currently, simulations using these methods have reported dynamics of few hundred of thousand RBCs [16,22,23], which is still far from physiological values in arterial system.

The need to develop an efficient method for cellular membrane has led to the emergent use of Dissipative Particle Dynamics (DPD) [27] in cellular flows. Pivkin et al. [20] and Fedosov et al. [21] proposed the state-of-the-art coarse-grained RBC-model based on the Dissipative Particle Dynamics approach. Following this method, only a few hundred particles are required to simulate the RBC dynamics. Therefore, the computational cost is reduced significantly. In this approach, both the fluid plasma and the cellular membrane, and the cytoplasm are simulated with the DPD method. To date, this coarse-grained DPD modeling has enabled a series of investigation of Red Blood Cell, White Blood Cell, and platelet in idealized models of vasculatures [15,28]. This DPD method is successful in simulating many behavior of the cells such as tank-treading and tumbling [29], deforming through a slit [25,30], or moving through stenosis collapse [31], or micro-fluidic devices [32]. However, the difficulty in resolving the interaction between fluid plasma and cell membrane remains a great challenge for DPD methods [15] since it is not clear how to assign physical values to DPD models of the fluid. As a particle-based method, the advantage of the DPD method is the flexibility in modeling complex fluids as the method satisfies conservation laws and other related constitutive equations [15]. However, there is a number of disadvantages for the DPD method such as the uncertain mechanism to set the physical values for governing parameters such as viscosity, density, and others. The DPD method only approximates fluid dynamics in the averaging sense (e.g., mean density and mean momentum). Therefore, it is challenging to apply the scaling arguments to the equations of motion for the DPD method. It is thus important to come up with a new method for simulating the fluid plasma separately from the RBC cytoskeleton dynamics.

Recognizing the challenges in coupling dynamics of cellular membranes and the fluid plasma, many numerical methods have been proposed to use different models for fluid plasma and the cell membrane [33] via the use of immersed boundary method. In this type of coupling, fluid plasma can be described separately from the cell membrane model. For example, Lattice Boltzmann Immersed Boundary Method has been also been developed [31,34,35]. In this model, the Lattice Boltzmann Method (LBM) [2], a particle-based method, is used to simulate the fluid plasma while the DPD or Finite Element model is used for the cell membrane. Other numerical methods for fluids have been proposed as well such as the Finite Element Method [36] or Finite Difference methods [17]. Particular roadblocks for this type of fluid-cell interaction coupling are: a) high computational cost to simulate individual cell dynamics; b) incompressibility constraint of the fluid plasma; and c) enforcing no-slip boundary condition of fluid flow in anatomical geometries of the arterial vasculature. These difficulties have been addressed separately in recent attempts [17,28,31] for a small domain. However, these are still major challenges if it is required to evaluate hemodynamics of a significantly large portion of the arterial tree such as the coronary arteries [22]. It is highly desired to devise a numerical strategy so that these roadblocks are removed with ease.

In this work, we propose a new approach based on the concept of continuum-particle coupling. The cell membrane is modeled using the coarse-grained particle approach (DPD) while the fluid plasma is simulated using continuum approach (sharp-interface immersed boundary method). The coupling of dynamics between the cell membrane and the fluid plasma is carried out using a Fluid-Structure Interaction (FSI) methodology. Such a combination allows the constraint of incompressibility of fluid plasma is satisfied while accommodating the FSI simulation of cells in anatomical geometries.

Our manuscript is organized as follows. First, we describe the essential components of the immersed boundary method for incompressible fluids in section 2.1. Second, the DPD methodology to simulate the dynamics of the lipid bi-layer membrane is explained in section 2.2. Third, the FSI methodology between the membrane and the fluid plasma is discussed in section 2.3. Finally, several numerical examples are investigated to examine the ability of the proposed framework for simulating RBC dynamics in different fluid flows in section 3. Discussions on the advantages and disadvantages of the proposed method will be shown in section 5.

2. Materials and Methods

2.1. Mathematical descriptions of the cell-fluid interaction using the sharp-interface immersed boundary method

The cell (erythrocyte) is considered a body Ω_s, which is immersed in a fluid Ω_f (blood plasma). The surface of the cell ($\partial\Omega_s$) is represented by a triangulated network [37]. The computational mesh for the fluid domain is therefore separated into two parts: a) the outer part Ω_f (blood plasma); and b) the inner part Ω_s as shown in Figure 1.

The dynamics of the cell is modeled via a Fluid-Structure Interaction (FSI) procedure since the cell deformation is under the impacts of the fluid forces and vice versa. Thus the cell and fluid motions are tracked simultaneously. On $\partial\Omega_s$ the no-slip boundary condition and the continuity of stresses are enforced. For the details of the coupling, the interested reader is referred to our previous publications [37,38]. Only essential components of the FSI methodology is discussed here.

The governing equations for the fluid motion in Ω_f is the Navier-Stokes equations. The Curvilinear Immersed Boundary method (CURVIB) [39] is used to solve the govering equation in curvilinear computational mesh. CURVIB uses the hybrid staggered/non-staggered approach [40] to solve the Navier-Stokes equations. Three-point central differencing are carried out for all spatial derivatives. Time integration is done via a second-order accurate fractional step method. The momentum equation are solved with a Jacobian-free solver while Flexible Generalized Minimal Residual ($FGMRES$) method with multigrid pre-conditioner is used to solve the Poisson equation to satisfy the discrete continuity equation to the machine-zero precision. Complex solid boundaries such as the membrane surface $\partial\Omega_s$ are handled using the sharp-interface immersed boundary method (IBM) with the velocity reconstruction along the local normal to the body [41] as shown in Figure 1. In this approach, the presence of a RBC in the fluid domain is substituted by the *immersed nodes* where the velocity reconstruction is carried out so that the no-slip boundary condition is satisfied on $\partial\Omega_s$ (green squares in Figure 1). The procedure to solve the fluid equations is denoted as the fluid solver $\mathfrak{F}$.

The CURVIB method is now implemented in the Virtual Flow Simulator (VFS), which is an open-source code and can be downloaded at http://safl-cfd-lab.github.io/VFS-Wind/. VFS has been applied for many problems in biological applications including brain aneurysms ([42–44], heart hemodynamics [45–47], and heart valves [48,49].

2.2. Membrane modeling

The RBC membrane is assumed to consist of a lipid bilayer attached to an inner cytoskeleton, which is a structure comprised by spectrin proteins and actins in a compact network. The cell's physical characteristics, such as the viscosity, the elasticity, and the bending stiffness, are derived fundamentally from these biological components. To mimic the interconnected structure of the cytoskeleton, the RBC membrane is modeled as a spring-network structure (a triangular mesh on a 2D surface), as described in the references [20,21]. Here, we follow the Dissipative Particle Dynamics approach [20,21,50] to simulate the dynamics of this network. The details of the computational methodology are as follows.

2.2.1. Red Blood Cell geometry and network triangulation

The shape of a normal RBC can be described using an analytical function [20]. The average shape of a RBC membrane [20,21] is given by a set of points with coordinates (x, y, z) in $3D$ space:

$$z = \pm D_0 \sqrt{1 - \frac{4(x^2+y^2)}{D_0^2}} \left[a_0 + a_1 \frac{x^2+y^2}{D_0^2} + a_2 \frac{(x^2+y^2)^2}{D_0^4} \right] \tag{1}$$

The parameters are chosen as $D_0 = 7.82\mu m$ (cell diameter), $a_0 = 0.00518$, $a_1 = 2.0026$, and $a_2 = -4.491$. The area and volume of this RBC are equal to $135(\mu m)^2$ and $94(\mu m)^3$, respectively (see also Table 1).

As the surface $\partial\Omega_s$ is known precisely according to the Equation 1, the triangulation procedure is carried out to mimic the distribution of the spectrin links on the membrane [20]. Using an open-source code (*distmeshsurface*) [51], the surface $\partial\Omega_s$ is triangulated with a predefined number of vertices N_v. The robustness of *distmeshsurface* allows it to generate a high-quality triangular meshes precisely on a 3D surface using a signed distance function.

2.2.2. Modeling the RBC membrane using the spectrin-link method

The membrane model is described by a two-dimensional triangulated network on a three-dimensional membrane surface Ω_s as shown in Figure 2a. The network is composed by a collection of points p_i with its Cartesian coordinates $\{x_i, y_i, z_i\}$ in Figure 2b. Here the index $i \in 1...N_v$ indicates the $i-th$ vertex of the surface triangulation. The vertices are connected in pairs by N_s springs (edges between the vertex i and j) forming N_t number of triangles.
All the equations presented in this work, describing the DPD model are taking directly from the work done by Pivkin et al. [20] and Fedosov et al. [21].

The internal forces ($\mathbf{f}_{internal}$) is related to the Helmholtz's free energy V as:

$$\mathbf{f}_{internal} = -\frac{\partial V}{\partial \mathbf{r}} \tag{2}$$

Here $\mathbf{r}$ is the position vector of the vertices.
The potential energy of the system includes the in-plane, bending, and area/volume constraints :

$$V(\{\mathbf{r}_i\}) = V_{in-plane} + V_{bending} + V_{area} + V_{volume} \tag{3}$$

The in-plane free energy term includes the elastic energy stored in the membrane. Here,the nonlinear wormlike-power $(WLC - POW)$ model [20] is used:

$$V_{in-plane} = \sum_{j \in 1...N_s} U_{WLC}(l_j) + \sum_{k \in 1...N_t} U_{POW}(l_j) \tag{4}$$

The wormlike chain (WLC) attractive potentials ($U_{WLC}(l_j)$) for individual links l_j is expressed as:

$$U_{WLC} = \frac{k_B T l_{max}}{4p} \frac{3x^2 - 2x^3}{1 - x} \tag{5}$$

where l_j is the length of the spring j, $x = \frac{l_j}{l_m}$ represents the spring deformation. l_{max} and p are the maximum length of the links and the persistence length, respectively. k_B and T are the Boltzmann's constant and the temperature, respectively.
The energy potential, U_{POW} [21], which defines a repulsive force in the form of a power function (POW). U_{POW} depends on the separation distance l_j as:

$$U_{POW}(l_j) = \frac{k_p}{(m-1) l_j^{m-1}} \quad m > 0,\ m \neq 1 \tag{6}$$

where k_p is the POW force coefficient and m is the exponent.

The bending energy $V_{bending}$ is defined as,

$$V_{bending} = \sum_{j \in 1...N_s} k_b [1 - cos(\theta_j - \theta_0] \tag{7}$$

Here k_b and θ_0 are the bending constant and the spontaneous angle, respectively. θ_j is the instantaneous angle between two adjacent triangles, which share the common edge (link) j as seen in Figure 2c.

The area and volume conservation constraints account for the incompressibility of the lipid bilayer and the inner cytosol, respectively. They are defined as:

$$\begin{aligned} V_{area} &= \frac{k_a (A - A_0^{tot})^2}{2A_0^{tot}} + \sum_{k \in 1...N_t} \frac{k_d (A_k - A_0)}{2A_0} \\ V_{volume} &= \frac{k_v (V - V_0^{tot})^2}{2V_0^{tot}} \end{aligned} \tag{8}$$

Here, A_k and A_0 is the instantaneous area of the k^{th} triangle (element) and the average area per element. k_a, k_d, and k_v are the global area, local area, and volume constraint coefficients, respectively. A and V are the instantaneous total

area and total volume of the RBC. The $A_0^{tot} = N_t A_0$ and V_0^{tot} are the specified total area and volume, respectively. The procedure to evaluate the values of V_{area} and V_{volume} is carried out from individual elements as shown in Figure 2.(b) [52]. In each triangle (element) of the network, three sides are established by linking the respective vertices 1, 2, and 3 as seen in Figure 2b. The length of the side connecting two vertices i and j (1,2, or 3) can be computed as $\mathbf{a}_{ij} = \mathbf{p}_i - \mathbf{p}_j$. Here $\mathbf{p}$ is the vector position of the vertex i or j ($i, j = 1, 2,$ *or* 3). The normal vector of the element $\boldsymbol{\zeta}$ can be derived from the cross product of $\mathbf{a}_{21}$ and $\mathbf{a}_{31}$ as shown in Figure 2(b) and (c). Note that the area and volume of a single triangle element can be also calculated from ζ as $A_k = \frac{|\boldsymbol{\zeta}|}{2} = \frac{\sqrt{\zeta_x^2+\zeta_y^2+\zeta_z^2}}{2}$ and $V_k = \frac{\boldsymbol{\zeta}^k \cdot \mathbf{t}_c^k}{6}$. Here $\mathbf{t}_c^k = \frac{\mathbf{p}_1^k+\mathbf{p}_2^k+\mathbf{p}_3^k}{3}$ is the position vector of the $k-th$ triangle centroid.

Finally, the internal force $f_{internal}$ contribution from $i-th$ vertex can be computed from the Equation (2) as:

$$\mathbf{f}^i_{internal} = \mathbf{f}^i_{WLC} + \mathbf{f}^i_{POW} + \mathbf{f}^i_{bending} + \mathbf{f}^i_{area_g} + \mathbf{f}^i_{area_{loc}} + \mathbf{f}^i_{volume} \tag{9}$$

2.2.3. Membrane viscosity

The RBC membrane is viscoelastic in nature. The membrane viscosity contribution is expressed as an additionally dissipative force as [52],

$$\mathbf{f}^D_{ij} = -\gamma^T \mathbf{v}_{ij} - \gamma^C \left(\mathbf{v}_{ij} \cdot \mathbf{e}_{ij}\right) \mathbf{e}_{ij} \tag{10}$$

where γ^T and γ^C are dissipative paramaters. Here the relative velocity between two adjacent vertices in the same link (i and j) is $\mathbf{v}_{ij} = \mathbf{v_i} - \mathbf{v_j}$. The position vector of the link is $\mathbf{e}_{i,j}$. The membrane viscosity is a function of both dissipative paramaters γ^T and γ^C. Here γ^T is responsible of a large portion of the membrane viscosity in comparison to γ^C. Following the suggestion of Fedosov et al. [52], γ^C is set to be equal to one third of γ^T. Consequently, these parameters relate to the physical viscosity of the membrane η_m as:

$$\begin{cases} \eta_m = \sqrt{3}\gamma^T + \dfrac{\sqrt{3}\gamma^C}{4} \\ \gamma^C = \dfrac{\gamma^T}{3} \end{cases}$$

So, the dissipative force of the membrane is:

$$\mathbf{f}^D_{ij} = -\frac{12}{13\sqrt{3}}\eta_m \mathbf{v}_{ij} - \frac{4}{13\sqrt{3}}\eta_m \left(\mathbf{v}_{ij} \cdot \mathbf{e}_{ij}\right) \mathbf{e}_{ij} \tag{11}$$

2.2.4. Coarse-graining procedure

A full-scale model of a RBC is typically consisted of millions of particles[53], which are required to simulate accurately protein dynamics. However, it is not feasible to use such a full-scale model in a FSI simulation due to the computational cost. In this work, we follow the coarse-graining procedure of Pivkin et al. [20] to represent the RBC membrane by a smaller number of particles (vertices). This procedure does not allow the detailed simulation of separate proteins but it is versatile enough to capture the overall dynamics of the RBC membrane.

Based on the equilibrium condition, Pivkin et al.[20] proposes a coarse-graining procedure based on the area/volume constraint for the spring equilibrium (l_0) and maximum (l_m) lengths as follows:

$$l_0^c = l_0^f \sqrt{\frac{N_v^f - 2}{N_v^c - 2}} \quad \text{and} \quad l_m^c = l_m^f \sqrt{\frac{N_v^f - 2}{N_v^c - 2}} \tag{12}$$

where the subscript c and f refer to the coarse-grained and the fine models, respectively.

Note that the role of l_0, l_m is critical in determining the response from the WLC model as seen in Equation 5. From the numerical standpoint, the RBC membrane model is highly sensitive with the value of l_0 and l_m.

As the number of vertices reduces, the average angle between the pairs of adjacent triangles increases. The spontaneous angle θ is adjusted in the coarse-grained model as [54]:

$$\theta_0^c = \theta_0^f \frac{N_v^f}{N_v^c} \quad \text{with} \quad \theta_0^f = \arccos\left(\frac{\sqrt{3}(N_v^f - 2) - 5\pi}{\sqrt{3}(N_v^f - 2) - 3\pi}\right) \tag{13}$$

Due to the scaling in Equation 12, the value of $x_0 = \frac{l_0}{l_m} = \frac{1}{2.2}$ does not change as the model is coarse-grained. To maintain the shear and area-compression moduli, the parameters p and k_p are adjusted as [21]:

$$p^c = p^f \frac{l_0^f}{l_0^c} \quad \text{and} \quad k_p^c = k_p^f \left(\frac{l_0^c}{l_0^f} \right)^{m+1} \tag{14}$$

The system of equations from (12) to (14) is used to calculate the coarse-grained parameters at the corresponding number of vertices N_v as shown in Table 1.

2.2.5. Scaling of model and physical units

One challenge in DPD modeling [28] is the relationship between the modeled quantities and the physical values since this relationship is not explicit. It is necessary to use a scaling argument to recover this relationship [21,29]. Here, the superscript M and P corresponds to the model and physical units (SI units), respectively.

The length scale (r^M) is defined as:

$$r^M = \frac{D_0^P}{D_0^M}, \tag{15}$$

r^M is the model unit of length. To be explicit, D_0^M is the cell diameter in the model unit and D_0^P is the physical cell diameter in meters.

The energy per unit mass($k_B T$) and the force N scaling values are given by:

$$\begin{aligned} (k_B T)^M &= \frac{Y^P}{Y^M} \left(\frac{D_0^P}{D_0^M} \right)^2 (k_B T)^P \\ N^M &= \frac{Y^P}{Y^M} \frac{D_0^P}{D_0^M} N^P \end{aligned} \tag{16}$$

with Y is the membrane Young's modulus. The timescale τ is defined as following:

$$\tau = \left(\frac{D_0^P}{D_0^M} \frac{\eta_m^P}{\eta_m^M} \frac{Y^M}{Y^P} \right)^{\alpha} \tag{17}$$

Here η_m is the membrane viscosity.

2.2.6. Time-integration scheme for the DPD model

The motion of each vertex i can be $i \in 1....N_v$ is described by the Newton's second law of motion:

$$M_i \frac{dv_i}{dt} = \mathbf{f}_{internal} + \mathbf{f}^i_{external} + \mathbf{f}^D_{ij} \;\; ; \quad \frac{dx_i}{dt} = v_i \tag{18}$$

where x_i, v_i are the position and the velocity of the vertex i, respectively. The mass per vertice M_i is defined as the mass per vertex $M_i = \frac{M}{N_v}$. The internal forces $\mathbf{f}_{internal}$ is computed from the Equation 9. Using the previous scaling methodology in section 2.2.5, the total mass of the RBC in the DPD model is set to be $M = 7.2 \times 10^{-12} kg$. Since the time scale is sufficiently small, we use the explicit Euler method to integrate the Equation 18 in time. The timestep Δt is chosen to be compatible with the FSI algorithm timestep.

The external forces $\mathbf{f}_{external}$ result from the fluid motion acting on the membrane. Therefore the traction vector $\mathbf{t}$ on $\partial\Omega_s$ must be evaluated from the fluid stress tensor σ_f as $\mathbf{t} = \sigma_f \boldsymbol{n}$. The normal vector of the surface at vertex i is $\boldsymbol{n}$. The details of σ_f evaluation has been explained in our previous work [37] extensively. In our method, the σ_f is computed directly from the fluid velocity and pressure field in the vicinity of the membrane. Note that the fluid velocity and pressure field are the solutions of the Navier Stokes equations in the domain Ω_f. In brief, the external forces $\mathbf{f}_{external}$ is evaluated as:

$$\mathbf{f}^i_{external} = \mathbf{t} S_i \tag{19}$$

Here S_i is the nodal area, which is the assigned area of the vertex i.

2.3. Fluid Structure Interaction methodology for cellular structures

The cellular structure ($\mathfrak{S}$) of section 2.2 is developed to simulate the membrane deformation in fluid flow. A FSI procedure is developed to link the dynamics of the cellular membrane with the fluid plasma using the immersed boundary method as described in section 2.1. The details of the FSI procedure has been developed and reported in our previous works [38]. To facilitate the discussion, we describe only the relevant aspects of our computational methodology as follows.

The deformable body (RBC-Ω_s) is immersed in the fluid plasma Ω_f as shown in Figure 1. The RBC membrane described in section 2.2 is the interface between Ω_s and Ω_f: $\Gamma_{RBC} = \partial\Omega_s = \bar{\Omega}_s \bigcap \bar{\Omega}_f$. The solid domain Ω_s deforms under the impacts of the fluid stresses. Our FSI algorithm is to determine the deformation of Γ_{RBC}.

Here the fluid plasma (Ω_f) is considered as a Newtonian incompressible fluid. The incompressible Navier-Stokes equations in section 2.1 are used to model the dynamics of the fluid plasma. The deformation of the solid body Ω_s is governed by the DPD model as described in section 2.2. On the one hand, the deformation of the RBC (Γ_{RBC}) is transferred to the flow field via the velocity field (Dirichlet boundary). On the other hand, the fluid stresses and the associated traction vector (Neumman boundary condition) are transferred from the fluid domain to the solid domain. The displacement field $\mathbf{d}$ of the N_v particles (vertices) can be found via a fixed-point iteration [see Reference 55, for example]:

$$\mathbf{d} = \mathfrak{F} \circ \mathfrak{S}(\mathbf{d}) \tag{20}$$

Here $\mathfrak{F}$ is the short-hand notation to describe the governing equations of the fluid domain while $\mathfrak{S}$ denotes the governing equations of the solid domain. The operator $\circ$ represents the load and displacement continuity conditions that are enforced on the interface Γ_{RBC}. Since this non-linear equation is typically stiff, different methods have been proposed to solve Equation 20 effectively. In the current work, fixed point iteration with relaxation (Aitken's acceleration) [41] is used to solve the Equation 20 for a time step $n+1$ from a known solution at the time step n.

3. Results

The dynamics of RBCs is investigated under different conditions: a) dynamic stretching under a pulling force; b) relaxing in a uniform flow; (c) deforming under shear flow in a confined tube; and d) moving through a curved tube. These tests will demonstrate the capability of the FSI methodology in modeling the interaction of a RBC with fluid flows.

3.1. Dynamics of RBC under stretching

Mills et al. [14] studied the deformation of a single Red Blood Cell under stretching with optical tweezers. The RBC is attached to two silica microbeads ($d = 4.12\mu m$) in a solution of Phosphate-Buffered Saline and Bovine Serum Albumin. Cell stretching is carried out by holding one microbead fixed while moving the other one with a force F. For each stretching test, the axial diameter (D_a) and the transverse diameter (D_t) are measured with the corresponding value of F. Here, the axial diameter D_a is defined along the direction of stretch. The transverse diameter D_t is measured in the orthogonal direction to the stretch direction. The definitions of D_a and D_t are shown in Figure 3. The experimental results of Mills et al. [14] are shown in Figure 4 with the error bounds indicating a significant variations of the D_t value.

To validate our RBC model, we perform the simulation of the stretching test of Mills et al. [14] following the suggestion of Pivkin et al. [20]. In our simulation, the applied force F locates axially from both sides within the contact area of the microbeads. In our simulation, the magnitude of the force F is incrementally increased from $0pN$ to $200pN$ in a step-wise manner (quasi-static) with the number of 16 steps in the total stretching period. The force is kept constant within each step so that the cell membrane has sufficient time to relax to a constant value. We perform our simulations with different values of vertices $N_v = 500, 1000, 3000, 9000, 27472$. The detailed values for each simulation are reported in Table 1.

Our results in Figure 4 show that the model replicates the RBC membrane dynamics reasonably well. The value of D_a in the proposed model agrees well with experimental data. However, the simulations underpredict the values of D_t across different N_v. Nevertheless, the simulated values of D_t are still in the upperbound of experimental values. Examining the shapes of the RBC under different values of F shows that the proposed model provide a consistent RBC shape across different values of vertices number N_v. As the stretching force is increased from 0 to $150pN$, the maximum length (D_a) and the minimum length (D_t) varies in a similar fashion of previous studies, both computations [20,21] and experiment [14]. Therefore, the robustness of the coarse-graining procedure has been demonstrated successfully. With only $N_v = 500$ vertices, the RBC membrane deformation shows a consistent behavior even in cases with much higher values of N_v. Unlike the continuum approaches, the DPD method is known to be insensitive to the mesh refinement

[20,21]. Therefore, choosing the appropriate value of N_v must balance between the computational cost and the required dynamics to be captured. Therefore, it is sufficient and economical to use the DPD model with $N_v = 500$ to represent the dynamics of RBC membrane as described below.

3.2. RBC deformation in a uniform flow (no shear)

Since the DPD model represents well the RBC dynamics under stretching as seen in section 3.1, it is reasonable to apply it into the FSI simulation. As the first step, FSI simulations are performed to test the sensitivity of the FSI methodology under zero shear stresses condition.

The RBC is positioned at the center of a computational domain, which is a rectangular domain of size $L_x = L_y = 10\ \mu m$ and $L_z = 45\ \mu m$ as shown in Figure 6. The computational domain is discretized with a uniform structured mesh with different grid sizes: a) Grid-1; b) Grid-2; and c) Grid-3 ranging from 50,000 thousand to 1.5 million grid points as shown in table 2. Since the coarse-grained DPD model $(N_v = 500)$ represents well the dynamics of the RBC membrane as discussed in section 3.1, it is used in this case. redIt is important to note that the spatial resolution of the structured mesh (Δx) must be able to resolve the RBC thickness. In addition, the spatial resolution of the triangular (unstructured) mesh of the RBC membrane should match the fluid mesh due to the requirement of the immersed boundary method. An uniform profile and the fully develop flow conditions are set at the inlet and outlet, respectively. Symmetry boundary conditions are set on other side planes.

First, the uniform inflow is linearly increased from 0 to a maximum velocity of $U_0 = 2mm/s$ at the inlet within $20\mu s$. After that, the uniform flow profile with U_0 is kept constant with time. Using the length scale of the cell diameter $D_0 = 7.82\mu m$ and the fluid viscosity of $\nu = 1.1 \times 10^{-6} m^2/s$, the maximum Reynolds number of the fluid domain Ω_f is calculated as $Re \approx 14.2 \times 10^{-3}$.In this case, the time scale of the DPD method (particles) is governed by the Equation 17. This time scale is smaller than the one required by the immersed boundary method. Therefore, the DPD time scale ($\Delta t = 1$ microsecond) is adopted in this work. Since the flow is uniform at very low Reynolds number, it is expected that the RBC deforms minimally and mostly propagates along the flow direction.

The dynamics of the RBC under the gradually increased load of the incoming flow at different time instances is shown in Figure 8. Initially, the shape of the RBC is set to be the analytical shape as discussed in section 2.2 at $t = 0$ as shown in Figure 7(a). However, the RBC starts to relax toward the stress-free condition as shown in Figure 7(b) and (c) after $400\mu s$. As the RBC shape reaches its equilibrium condition, it translate along the flow direction (x).

The results of the grid refinement study are shown in Figure 8. The shape of the simulated RBC is compared across different sizes of the fluid mesh (see Table 2) on the x symmetry plane at $t = 240\mu s$. It is shown that the RBC shapes agree well with each other. Therefore, the proposed numerical method for FSI simulation of RBC is consistent.

3.3. Fluid-Structure Interaction simulation of an immersed RBC in a confined tube

To illustrate the capabilities and robustness of the proposed model under shear flow, we replicate the simulation procedure proposed by Pivkin et al [20]. The computational domain resembles the Poiseuille flow with the tube diameter of $D = 10\mu m$ as shown in Figure 9. The RBC is initially placed at the center of the domain. Here we also use the coarse-grained DPD model with $N_v = 500$ as discussed in Table 1.

A time-varied uniform inflow profile is prescribed at the inlet $U(t)$. The value of $U(t)$ is linearly increased from 0 to a maximum velocity of $U_0 = 2mm/s$ at the inlet within $20\mu s$. After that, the uniform flow profile with $U(t) = U_0$ is kept constant with time. Using the length scale of the pipe diameter $D = 10\mu m$ and the fluid viscosity of $\nu = 1.1 \times 10^{-6} m^2/s$, the bulk Reynolds number of the problem is $Re \approx 18.2 \times 10^{-3}$. At the outlet, the Neumman boundary condition is applied. On the pipe wall, no-slip condition is enforced.

As the pressure gradient develops inside the tube, the RBC starts to deform as shown in Figure 11(a) (top row). Initially, it has the biconcave shape as discussed in section 2.2. However, its transitions from the initial biconcave shape to a parachute shape within $1ms$. The transition is remarkable given that one side of the RBC membrane is pulled forward significantly. After this transition, the RBC propagates along the tube axis with minimal changes in its shape. Note that this phenomenon is widely observed in *in-vitro* experiments [56] and discussed extensively in literature [17,52]. During this process, the flow field inside the tube resembles closely the parabolic profile, except in the vicinity of the RBC membrane as illustrated in Figure 11(b) (bottom row). In brief, the FSI methodology accurately predicts the shape transition of the RBC in Poiseuille flow.

To examine the potential impacts of the triangular mesh resolution, two additional simulations are carried out with $N_v = 1000$ and $N_v = 3000$ as shown in Figure 10. Comparing between the case of $N_v = 500$ and $N_v = 1000$ in Figure 10(a) and (b), it is shown that the transition to the parachute shape is delayed in $N_v = 1000$. The membrane seems to become stiffer with the larger value of N_v. However, the differences of the RBC dynamics between the cases $N_v = 1000$

and $N_v = 3000$ are minimal. The RBC shapes for the refined cases ($N_v = 1000$ and $N_v = 3000$) are nearly identical as depicted in Figure 10(b) and (c). These results indicate that it is required at least $N_v = 1000$ to reflect the RBC dynamics in micro-vessels accurately.

3.4. RBC migration in an artery model

To illustrate the capability of the proposed method for flows in micro-vasculature, FSI simulation of a RBC in a curved tube is carried out as shown in Figure 12. The fluid domain is created as a curved tube of $12\mu m$ in diameter with arbitrary curvature. The tube (computational domain) is discretized with a structured grid of size $81 \times 81 \times 141$ with the approximate spacing $0.2\mu m \times 0.17\mu m \times 0.54\mu m$ in the (i, j, k) directions, respectively. The RBC model ($N_v = 500$) is initially placed at a distance of $20\mu m$ from the inlet.

Similar to the previous cases, a time-varied uniform inflow profile is prescribed at the inlet $U(t)$. The value of $U(t)$ is linearly increased from 0 to a maximum velocity of $U_0 = 2mm/s$ at the inlet within $20\mu s$. After that, the uniform flow profile with $U(t) = U_0$ is kept constant with time. Using the length scale of the pipe diameter $D = 12\mu m$ and the fluid viscosity of $\nu = 1.1 \times 10^{-6} m^2/s$, the bulk Reynolds number of the problem is $Re \approx 21.8 \times 10^{-3}$. At the outlet, the Neumman boundary condition is applied. On the tube wall, no-slip condition is enforced. The RBC starts to deform in the as shown in Figure 13 , following the same deformation patterns in the previous case of a straight tube. One side of the cell is pulled strongly to achieve the parachute shape in almost the same time window of 1 ms. However, the shape of the RBC is not completely symmetric as one in the straight tube. Here, the tube curvature slightly impacts the deformation so that the RBC shape depends on the local curvature of the tube. In brief, the DPD model is able to respond to the local features of the complex flow in micro-channel geometries.

4. Discussions

To our knowledge, the coupling of a continuum approach, such as the Immersed Boundary Method, and the particles systems of Dissipative Particle Dynamics, has never been carried out before. The novelty of our approach leads to several numerical advantages: i) satisfying the no-slip boundary condition on the cell surface; ii) ensuring the incompressibility of the fluid plasma; and iii) being flexible in handling anatomical geometries. The details of such advantages are explained below.

Due to the sharp-interface nature of the approach, the no-slip boundary condition on the cell surface can be satisfied easily. The sharp-interface immersed boundary method [40] ensures that the velocity in the closest fluid point (immersed nodes - see Figure 1) is reconstructed by interpolating between the flow field and the motion of the membrane surface. In our approach, the Navier-Stokes equations are the governing equations for the fluid plasma. Hence, the incompressibility constraint is satisfied exactly for the fluid domain, which is not possible if particle-based methods such as LBM or DPD are used [33]. This incompressibility condition is important since it ensures an accurate estimation of the fluid shear stresses. Moreover, the use of immersed boundary method simplifies the procedure to incorporate anatomical geometries of the arteries in our future works. This feature will be useful in simulating blood flow in arterioles and veins. In brief, our proposed method improves the accuracy of RBC dynamics simulations without increasing the computational cost significantly.

The state-of-the-art numerical methods for cellular flows are currently limited by the computational expense of resolving individual RBC dynamics (e.g few hundred of thousands cells) [16,22,23]. Therefore, a computationally expedient algorithm will enable simulation of cellular dynamics under physiological conditions. The use of DPD for RBC dynamics has been popularized [20,21] because the lipid bilayer and the cytoskeleton mechanics can be described easily using a set of particles, which represents the cytoskeletal structure. Our results in section 3.1 show that DPD is efficient and robust in simulating RBC deformation under a large range of impacting forces. This is remarkable given that the DPD model is much simpler in comparison to elaborated methods such as the FEM [17,36]. With only $N_v = 500$ particles, our results show that DPD model yields cellular deformation in good agreement with previous computational and experimental data [14,17,20,21,57]. All simulations were performed with a relatively inexpensive computational cost. The computational cost of the DPD is negligible in comparison to the fluid flow solver using the immersed boundary method. Overall, each simulation requires 20 CPUs and 20Gb RAM to run in approximately 24 hours wall clock time.

We follow the original DPD model of Pivkin et al. [20]. In this model, the mass of RBC is set to be 7.2×10^{-12} kg according to the force and length scales proposed by Pivkin et al. [20]. However, the real mass of one RBC varies from $M = 27.2 - 121 \times 10^{-15} kg$ [58]. So, there is a significant difference in the modeled and the real mass of the RBC. Our future work will investigate the dependence of stability condition on the RBC mass.

The immersed boundary method has been used to simulate dynamics of RBC in fluid flow in previous works [17,59] mostly in the context of diffuse interface. The membrane/fluid interface is typically tracked via a level-set approach

[17], which ensures the continuity of viscosity distribution [23]. This diffusive interface approach does not allow a sharp distinction (or jump condition) of fluid properties from the inner and outer parts of the cell. Our approach allows the further development of a more complex model for RBC [19] since the RBC model is completely independent on the fluid model. Past works have ignored the dynamics role of cytosol [20]. Our approach can be easily extended to include this effect by developing a separate model for the cytosol. Furthermore, many other processes have not been considered in the current model such as the cell-cell interaction [31] and the cell-vascular wall interaction [2]. Our future efforts will further extend the framework to include such aspects.

In brief, our proposed method has several limitations. First, it is challenging for the DPD method to set the important physical parameters such as the viscosity and the density of the RBC membrane independently. Second, the implementation of the immersed boundary method requires the continuous tracking of the RBC surface. In the current work, there is only one RBC is simulated so the computational cost is negligible. However, a physiological condition in human arterioles might include millions of RBCs. Therefore, a special algorithm to accommodate such a tracking should be developed in future. Third, the interaction between RBCs and the arterial wall must be simulated in a realistic condition. Therefore, a model for the collisions between the cells and the vascular walls should be developed. Our future work will explore the use of the Morse Potential [30,31] to achieve this end.

5. Conclusions

In this work, we have developed a new coupling approach between the sharp-interface immersed boundary method and the Dissipative Particle Dynamics to simulate dynamics of cells in fluid flows. This hybrid continuum-particle method is then applied to simulate transport of Red Blood Cell in a straight and curved tubes. Our results show good agreements with experimental measurements as well as other computational works. Our results show that the new formulation is highly efficient in computing the deformation of cells within fluid flow while satisfying the incompressibility constraints of the fluid locally. This feature is critical for an estimation of fluid shear stresses on the surface of RBC as well as the vascular walls. Therefore, our proposed approach can be applied for many biomedical applications such as estimating the fluctuations of RBC membrane [53], thrombus formation, blood clots [30,31]. Our results also suggest that this hybrid methodology can be extended for a variety of cells in physiological conditions such as the dynamics of white blood cells, platelets, or cancer cells [35]. Our future works will extend the current framework to be applicable for such situations.

Author Contributions: Conceptualization, T.L; methodology, T.L.; software, L.A.; validation, L.A.; formal analysis, T.L. L.A.; investigation, L.A.; resources, T.L.; data curation, T.L. L.A; writing—original draft preparation, T.L. L.A.; writing—review and editing, L.A.; visualization, T.L.; supervision, T.L.; project administration, T.L.; funding acquisition. All authors have read and agreed to the published version of the manuscript.

Funding: This project is supported by NSF grant number 1946202 (New Discoveries in the Advanced Interface of Computation, Science, and Engineering:ND-ACES) and ND EPSCOR project FAR0030612. This work is partially supported by the start-up package of Trung Bao Le from the Department of Civil and Environmental Engineering, North Dakota State University, United States.

Institutional Review Board Statement: Not applicable

Informed Consent Statement: Not applicable

Data Availability Statement: Please refer to suggested Data Availability Statements in section "MDPI Research Data Policies" at https://www.mdpi.com/ethics.

Acknowledgments: The computational works were performed using the computational resources of Center for Computationally Assisted Science and Technology (CCAST) at North Dakota State University. This work also used the Extreme Science and Engineering Discovery Environment (XSEDE) Bridges at the Pittsburg Supercomputing Center through allocation CTS190053.

Conflicts of Interest: The authors declare no conflict of interest. The funders had no role in the design of the study; in the collection, analyses, or interpretation of data; in the writing of the manuscript, or in the decision to publish the results

Abbreviations

The following abbreviations are used in this manuscript:

DPD	Dissipative Particle Dynamics
SPH	Smooth Particle Hydrodynamics
LBM	Lattice Boltzman Method
IBM	Immersed Boundary Method
FSI	Fluid-Structure Interaction

References

1. Hobson, C.M.; Stephens, A.D. Modeling of Cell Nuclear Mechanics: Classes, Components, and Applications. *Cells* **2020**, *9*, 1623.
2. Dabagh, M.; Gounley, J.; Randles, A. Localization of Rolling and Firm-Adhesive Interactions Between Circulating Tumor Cells and the Microvasculature Wall. *Cellular and Molecular Bioengineering* **2020**, pp. 1–14.
3. Mehrabadi, M.; Ku, D.N.; Aidun, C.K. A continuum model for platelet transport in flowing blood based on direct numerical simulations of cellular blood flow. *Annals of biomedical engineering* **2015**, *43*, 1410–1421.
4. Mauer, J.; Mendez, S.; Lanotte, L.; Nicoud, F.; Abkarian, M.; Gompper, G.; Fedosov, D.A. Flow-Induced Transitions of Red Blood Cell Shapes under Shear. *Phys. Rev. Lett.* **2018**, *121*, 118103. doi:10.1103/PhysRevLett.121.118103.
5. L. L. Xiao, S. Chen, .S.L.; Liu, Y. Highly resolved pulsatile flows through prosthetic heart valves using the entropic lattice-Boltzmann method. *Molecular Cellular Biomechanics* **2014**, *11*, 67–85.
6. Müller, S.J.; Weigl, F.; Bezold, C.; Bächer, C.; Albrecht, K.; Gekle, S. A hyperelastic model for simulating cells in flow. *Biomechanics and Modeling in Mechanobiology* **2020**, pp. 1–12.
7. Hynes, W.F.; Pepona, M.; Robertson, C.; Alvarado, J.; Dubbin, K.; Triplett, M.; Adorno, J.J.; Randles, A.; Moya, M.L. Examining metastatic behavior within 3D bioprinted vasculature for the validation of a 3D computational flow model. *Science Advances* **2020**, *6*, [https://advances.sciencemag.org/content/6/35/eabb3308.full.pdf]. doi:10.1126/sciadv.abb3308.
8. Lenarda, P.; Coclite, A.; Decuzzi, P. Unraveling the vascular fate of deformable circulating tumor cells via a hierarchical computational model. *Cellular and Molecular Bioengineering* **2019**, *12*, 543–558.
9. Liu, Z.L.; Clausen, J.R.; Wagner, J.L.; Butler, K.S.; Bolintineanu, D.S.; Lechman, J.B.; Rao, R.R.; Aidun, C.K. Heterogeneous partition of cellular blood-borne nanoparticles through microvascular bifurcations. *Physical Review E* **2020**, *102*, 013310.
10. Marcel Akpa Agnero, Kouakou Konan, Z.G.C.S.T.Y.T.A.K.B.S.D.K.A.K.; Zoueu, J.T. Malaria-Infected Red Blood Cell Analysis through Optical and Biochemical Parameters Using the Transport of Intensity Equation and the Microscope's Optical Properties **2019**.
11. Shabnam A. Faraghata, Kai F. Hoettgesa, M.K.S.D.R.v.d.V.W.J.B.E.A.H.F.H.L.; Hughesa, M.P. High-throughput, low-loss, low-cost, and label-free cell separation using electrophysiology-activated cell enrichment **2017**. *114*, 4591–4596.
12. Muzykantov, V.R. Drug delivery by red blood cells: vascular carriers designed by Mother Nature **2010**. *7*, 406–428.
13. H. W. Hou, A. A. S. Bhagat, W.C.L.S.H.J.Y.H.C.T.L. Microfluidic Devices for Blood Fractionation, Micromachines. **2011**. *2*, 319–343.
14. J.P. Mills, L. Qie, M.D.C.L.; Suresh, S. Nonlinear Elastic and Viscoelastic Deformation of the Human Red Blood Cell withOptical Tweezers. *Mech. Chem. Biosys* **2004**, *1*, 169–180.
15. Ye, T.; Phan-Thien, N.; Lim, C.T. Particle-based simulations of red blood cells—A review. *Journal of biomechanics* **2016**, *49*, 2255–2266.
16. Kotsalos, C.; Latt, J.; Beny, J.; Chopard, B. Digital blood in massively parallel CPU/GPU systems for the study of platelet transport. *Interface Focus* **2021**, *11*, 20190116.
17. Balogh, P.; Bagchi, P. A computational approach to modeling cellular-scale blood flow in complex geometry. *Journal of Computational Physics* **2017**, *334*, 280–307.
18. Li, J.; Dao, M.; Lim, C.; Suresh, S. Spectrin-level modeling of the cytoskeleton and optical tweezers stretching of the erythrocyte. *Biophysical journal* **2005**, *88*, 3707–3719.
19. Tang, Y.H.; Lu, L.; Li, H.; Evangelinos, C.; Grinberg, L.; Sachdeva, V.; Karniadakis, G.E. OpenRBC: A fast simulator of red blood cells at protein resolution. *Biophysical journal* **2017**, *112*, 2030–2037.
20. Pivkin, I.V.; Karniadakis, G.E. Accurate coarse-grained modeling of red blood cells. *Physical review letters* **2008**, *101*, 118105.
21. Fedosov, D.A.; Caswell, B.; Karniadakis, G.E. A multiscale red blood cell model with accurate mechanics, rheology, and dynamics. *Biophysical journal* **2010**, *98*, 2215–2225.
22. Lu, L.; Morse, M.J.; Rahimian, A.; Stadler, G.; Zorin, D. Scalable simulation of realistic volume fraction red blood cell flows through vascular networks. Proceedings of the International Conference for High Performance Computing, Networking, Storage and Analysis, 2019, pp. 1–30.
23. Saadat, A.; Guido, C.J.; Iaccarino, G.; Shaqfeh, E.S. Immersed-finite-element method for deformable particle suspensions in viscous and viscoelastic media. *Physical Review E* **2018**, *98*, 063316.
24. Freund, J.B. The flow of red blood cells through a narrow spleen-like slit. *Physics of Fluids* **2013**, *25*, 110807, [https://doi.org/10.1063/1.48193 doi:10.1063/1.4819341.
25. Lu, H.; Peng, Z. Boundary integral simulations of a red blood cell squeezing through a submicron slit under prescribed inlet and outlet pressures. *Physics of Fluids* **2019**, *31*, 031902.
26. Park, S.Y.; Dimitrakopoulos, P. Transient dynamics of an elastic capsule in a microfluidic constriction. *Soft Matter* **2013**, *9*, 8844–8855. doi:10.1039/C3SM51516H.
27. Hoogerbrugge, P.J.; Koelman, J.M.V.A. Simulating Microscopic Hydrodynamic Phenomena with Dissipative Particle Dynamics. *EPL (Europhysics Letters)* **1992**, *19*, 155–160.
28. Ye, T. Pan, D. Huang, C. Liu, M.Smoothed particle hydrodynamics (SPH) for complex fluid flows: Recent developments in methodology and applications. *Physics of Fluids* **2019**, *31*, 011301, [https://doi.org/10.1063/1.5068697]. doi:10.1063/1.5068697.
29. Peng, Z.; Li, X.; Pivkin, I.V.; Dao, M.; Karniadakis, G.E.; Suresh, S. Lipid bilayer and cytoskeletal interactions in a red blood cell. *Proceedings of the National Academy of Sciences* **2013**, *110*, 13356–13361.

30. Xiao, L.; Liu, Y.; Chen, S.; Fu, B. Numerical simulation of a single cell passing through a narrow slit. *Biomechanics and modeling in mechanobiology* **2016**, *15*, 1655–1667.
31. Xiao, L.; Lin, C.; Chen, S.; Liu, Y.; Fu, B.; Yan, W. Effects of red blood cell aggregation on the blood flow in a symmetrical stenosed microvessel. *Biomechanics and Modeling in Mechanobiology* **2020**, *19*, 159–171.
32. Deng, Y.; Papageorgiou, D.P.; Li, X.; Perakakis, N.; Mantzoros, C.S.; Dao, M.; Karniadakis, G.E. Quantifying Fibrinogen-Dependent Aggregation of Red Blood Cells in Type 2 Diabetes Mellitus. *Biophysical journal* **2020**, *119*, 900–912.
33. Freund, J.B. Numerical simulation of flowing blood cells. *Annual review of fluid mechanics* **2014**, *46*, 67–95.
34. Yin, X.; Thomas, T.; Zhang, J. Multiple red blood cell flows through microvascular bifurcations: Cell free layer, cell trajectory, and hematocrit separation. *Microvascular Research* **2013**, *89*, 47 – 56. doi:https://doi.org/10.1016/j.mvr.2013.05.002.
35. Dabagh, M.; Randles, A. Role of deformable cancer cells on wall shear stress-associated-VEGF secretion by endothelium in microvasculature. *PLOS ONE* **2019**, *14*, 1–15. doi:10.1371/journal.pone.0211418.
36. Casquero, H.; Bona-Casas, C.; Toshniwal, D.; Hughes, T.J.; Gomez, H.; Zhang, Y.J. The divergence-conforming immersed boundary method: Application to vesicle and capsule dynamics. *Journal of Computational Physics* **2021**, *425*, 109872. doi:https://doi.org/10.1016/j.jcp.2
37. Gilmanov, A.; Le, T.B.; Sotiropoulos, F. A numerical approach for simulating fluid structure interaction of flexible thin shells undergoing arbitrarily large deformations in complex domains. *Journal of Computational Physics* **2015**, *300*, 814–843. doi:https://doi.org/10.1016/j.jcp.2015.08.008.
38. Le, T.B.; Christenson, A.; Calderer, T.; Stolarski, H.; Sotiropoulos, F. A thin-walled composite beam model for light-weighted structures interacting with fluids. *Journal of Fluids and Structures* **2020**, *95*, 102968. doi:https://doi.org/10.1016/j.jfluidstructs.2020.102968.
39. Ge, L.; Sotiropoulos, F. A numerical method for solving the 3D unsteady incompressible Navier–Stokes equations in curvilinear domains with complex immersed boundaries. *Journal of computational physics* **2007**, *225*, 1782–1809.
40. Gilmanov, A.; Sotiropoulos, F. A hybrid Cartesian/immersed boundary method for simulating flows with 3D, geometrically complex, moving bodies. *Journal of computational physics* **2005**, *207*, 457–492.
41. Borazjani, I.; Ge, L.; Sotiropoulos, F. Curvilinear immersed boundary method for simulating fluid structure interaction with complex 3D rigid bodies. *Journal of Computational physics* **2008**, *227*, 7587–7620.
42. Le, T.B.; Borazjani, I.; Sotiropoulos, F. Pulsatile flow effects on the hemodynamics of intracranial aneurysms. *Journal of biomechanical engineering* **2010**, *132*.
43. Le, T.B.; Troolin, D.R.; Amatya, D.; Longmire, E.K.; Sotiropoulos, F. Vortex phenomena in sidewall aneurysm hemodynamics: experiment and numerical simulation. *Annals of biomedical engineering* **2013**, *41*, 2157–2170.
44.
45. Le, T.B.; Sotiropoulos, F. On the three-dimensional vortical structure of early diastolic flow in a patient-specific left ventricle. *European Journal of Mechanics-B/Fluids* **2012**, *35*, 20–24.
46. Le, T.B.; Sotiropoulos, F.; Coffey, D.; Keefe, D. Vortex formation and instability in the left ventricle. *Physics of Fluids* **2012**, *24*, 091110.
47. Le, T.B.; Elbaz, M.S.; Van Der Geest, R.J.; Sotiropoulos, F. High Resolution Simulation of Diastolic Left Ventricular Hemodynamics Guided by Four-Dimensional Flow Magnetic Resonance Imaging Data. *Flow, Turbulence and Combustion* **2019**, *102*, 3–26.
48. Le, T.B.; Sotiropoulos, F. Fluid–structure interaction of an aortic heart valve prosthesis driven by an animated anatomic left ventricle. *Journal of computational physics* **2013**, *244*, 41–62.
49. Sotiropoulos, F.; Le, T.B.; Gilmanov, A. Fluid mechanics of heart valves and their replacements. *Annual Review of Fluid Mechanics* **2016**, *48*, 259–283.
50. Oursler, S.M. A Proposed Mechanical-Metabolic Model of the Human Red Blood Cell. PhD thesis, 2014.
51. Persson, P.O.; Strang, G. A Simple Mesh Generator in MATLAB. *SIAM Review* **2004**, *46*, 329–345.
52. Fedosov, D.; Caswell, B.; Karniadakis, G. Dissipative particle dynamics modeling. *Computational hydrodynamics of capsules and biological cells* **2010**, p. 183.
53. Yu-Hang Tang, Lu Lu, H.L.C.E.L.G.V.S.; Karniadakis, G.E. OpenRBC: A Fast Simulator of Red Blood Cells at Protein Resolution **2017**. *112*, 2030–2037.
54. Fedosov, D.A. Multiscale Modeling of Blood Flow and Soft Matter **2010**.
55. Degroote, J.; Haelterman, R.; Annerel, S.; Bruggeman, P.; Vierendeels, J. Performance of partitioned procedures in fluid–structure interaction. *Computers & structures* **2010**, *88*, 446–457.
56. G. Tomaiuolo, V. Preziosi, M.S.S.G.R.C.V.M.C.R.; Rotoli, B. A methodology to study the deformability of red blood cells flowing in microcapillaries in vitro **2007**. *43*, 186–192.
57. Dao, M.; Lim, C.T.; Suresh, S. Mechanics of the human red blood cell deformed by optical tweezers. *Journal of the Mechanics and Physics of Solids* **2003**, *51*, 2259–2280.
58. Phillips, K.G.; Jacques, S.L.; McCarty, O.J. Measurement of single cell refractive index, dry mass, volume, and density using a transillumination microscope. *Physical review letters* **2012**, *109*, 118105.
59. Sigüenza, J.; Mendez, S.; Ambard, D.; Dubois, F.; Jourdan, F.; Mozul, R.; Nicoud, F. Validation of an immersed thick boundary method for simulating fluid–structure interactions of deformable membranes. *Journal of Computational Physics* **2016**, *322*, 723 – 746. doi:https://doi.org/10.1016/j.jcp.2016.06.041.

N_v	D_0^M	$l_0\ (m)$	$l_m\ (m)$	$p\ (m)$	$\theta_0\ (deg)$
500	8.06	5.5614×10^{-7}	1.2235×10^{-6}	1.9933×10^{-9}	6.86
1000	8.07	3.7992×10^{-7}	8.3582×10^{-7}	2.9179×10^{-9}	4.69
3000	8.07	2.2818×10^{-7}	5.0199×10^{-7}	4.8584×10^{-9}	2.82
9000	8.12	1.3035×10^{-7}	2.8678×10^{-7}	8.5044×10^{-9}	1.61
27472	8.26	7.5331×10^{-8}	1.6573×10^{-7}	1.4716×10^{-8}	0.93

Table 1: DPD parameters for the model of RBC membrane for different number vertices N_v. D_0^M is the model length scale, l_0 is the equilibrium length of the links, l_m is the maximum length of the links, p is the persistence length and θ_0 is the spontaneous angle. In these cases, $k_a = 4900$, $k_d = 100$, $k_v = 5000$, $A_0^{tot} = 135 \times 10^{-12} m^2$, and $V_0^{tot} = 94 \times 10^{-18} m^3$, respectively. Other parameters are $\alpha = 1$, $\eta_m^P = 6 \times 10^{-3} Ns/m^2$ and $\eta_m^M = 1.8$.

Grid	**Size**	$\mathbf{\Delta x \times \Delta y \times \Delta z}\ (\mu m)$	**Total grid points**
1	$31 \times 31 \times 51$	$0.44 \times 0.42 \times 0.9$	49,011
2	$81 \times 81 \times 101$	$0.17 \times 0.14 \times 0.45$	662,661
3	$101 \times 101 \times 151$	$0.16 \times 0.10 \times 0.3$	1,540,351

Table 2: Grid refinement study for the FSI simulation of a single RBC in uniform flow. The RBC is simulated with the coarsest DPD model ($N_v = 500$) as seen in Table 1. The domain $(-5:5, -5:5, -22.5:22.5)\mu m$ is discretized as a structured grid with uniform spacing in (x, y, z) directions as shown in Figure 6.

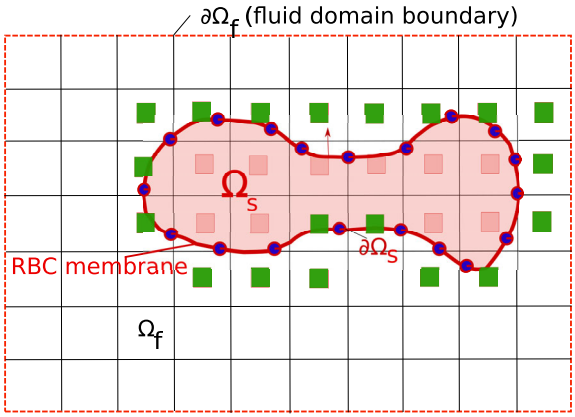

Figure 1. The representation of the RBC inside the fluid plasma using the immersed boundary method (IBM). The RBC membrane is the surface of the solid domain ($\partial\Omega_s$), which is depicted as a line connected by blue circles. The fluid domain is denoted as Ω_f with the appropriate boundary conditions $\partial\Omega_f$. The green squares represent the immersed nodes, which are the adjacent nodes to the cell surface $\partial\Omega_s$. The no-slip boundary condition is enforced on $\partial\Omega_s$

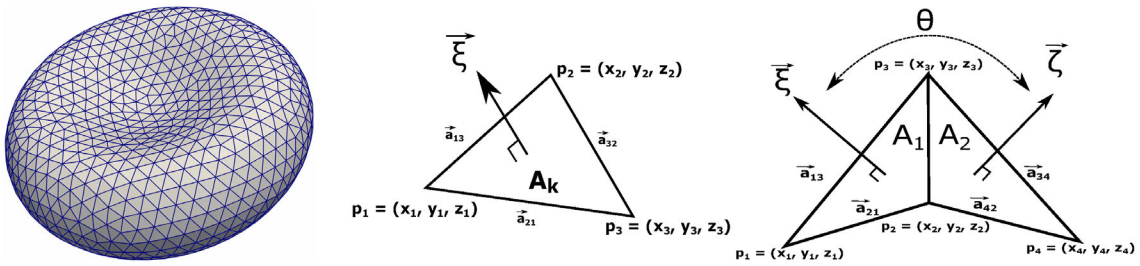

(a) (b)

Figure 2. (a). The triangulated surface of the spectrin network attached to the lipid bilayer membrane. The numbers of vertices and triangles are denoted as N_e and N_v. The number of vertices varies from $N_v = 500$ to $N_v = 27,344$ points (nodes). (b) The definition of the normal surface vector ζ and the spontaneous angle θ between two adjacent elements. A element is defined by three vertices (p_1, p_2, p_3) of the triangulated network.

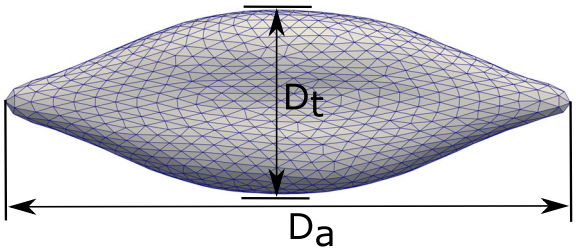

Figure 3. The definitions of the axial diameter (D_a) and the traverse direction (D_t). The deformation of the RBC is measured by the quantities D_a and D_t as shown in Figure 4

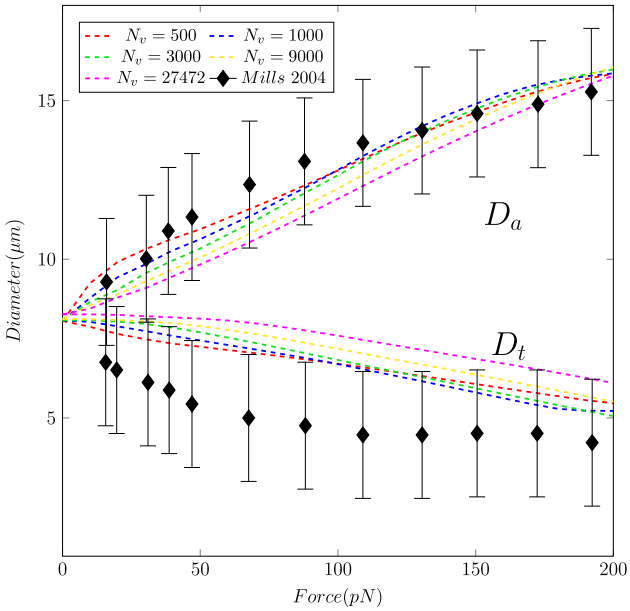

Figure 4. The evolution of the axial and transverse diameters (D_a and D_t) of the RBC versus stretching force F. The experimental data from [14] is shown with black line with error bounds. The coarse-graining simulations are shown with lines: red ($N_v = 500$), blue ($N_v = 1000$), green ($N_v = 3000$), yellow ($N_v = 9000$), and magenta ($N_v = 27472$).

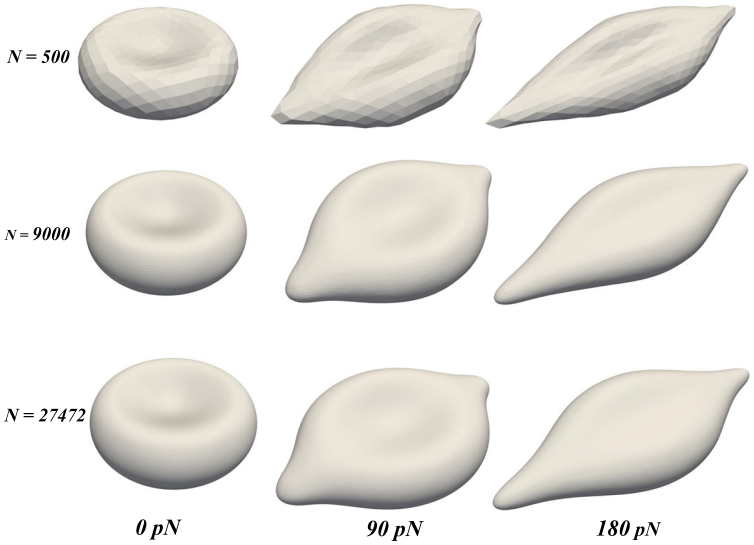

Figure 5. The deformation of the RBC membrane under stretching force F with different values of N_v: 500 (top row), 9000 (middle row), and 27472 (bottom row). Three time instants (see Figure 3) are chosen to demonstrate the dynamics: 0pN (left column), 90pN (middle column), and 180pN (right column).

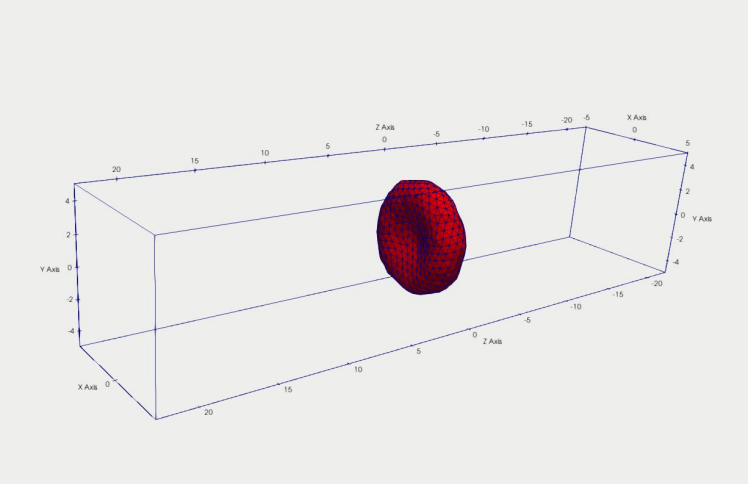

Figure 6. Computational setup for the Fluid-Structure Interaction simulation of a single RBC in uniform flow. The computational domain is a structured mesh of size $10\mu m \times 10\mu m \times 45\mu m$. The uniform flow (no shear) is applied at the (x-y) plane of $z = -22.5\mu m$. The Neumman boundary condition is applied at the outlet. Symmetry (slip) boundary condition is applied in other sides. The RBC is initially placed at the center of the computational domain $z = 0$.

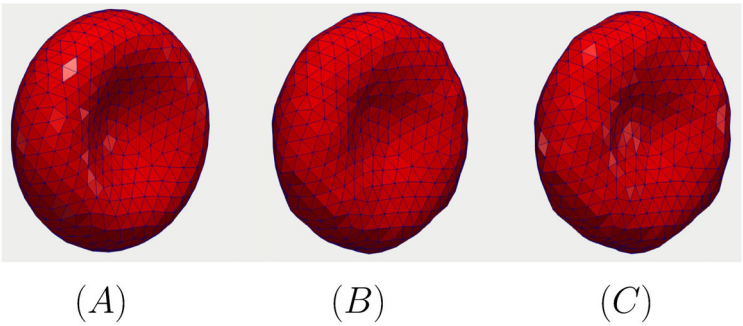

Figure 7. The relaxation of the RBC under zero-shear condition. The initial shape of the RBC is the analytical shape as discussed in section 2.2 at $t = 0$ (A). The RBC relaxes toward the stress-free condition in (B) ($t = 200\mu s$) and (C) ($t = 400\mu s$). The results are taken from the Grid-1 simulation as indicated in Table 2.

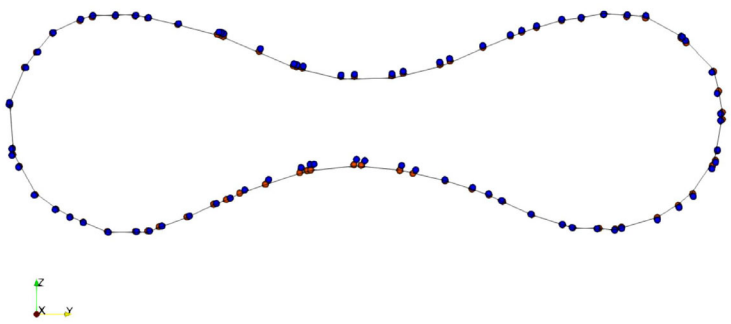

Figure 8. The impacts of computational mesh size on the simulated results of RBC deformation. The shape of the RBC membrane is shown in a symmetry plane orthogonal to the x direction at the time instance of $240\mu s$. The position of the vertices of the RBC in Grid-1, Grid-2, and Grid-3 (see Table 2)are shown in blue points, red points, and the solid line, respectively. The shape of the RBC is nearly identical under different computational grids.

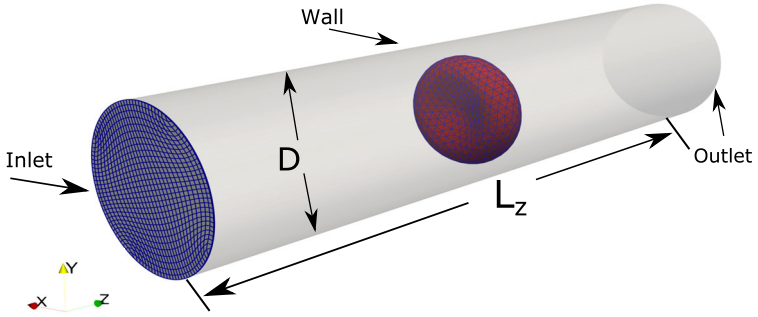

Figure 9. Computational setup for the Fluid-Structure Interaction simulation between a single RBC in Poiseuille flow. The computational domain (the tube) is a structured mesh of size $31 \times 31 \times 51$ with the average spacing in the (i, j, k) directions are approximately $0.4\mu m \times 0.4\mu m \times 0.9\mu m$. The curvilinear mesh at the $k = 0$ plane is shown in blue for an illustration of the computational mesh. Time-varied uniform flow is prescribed at the inlet at $k = 0$. The fully developed boundary is applied at the outlet. Wall boundary (no-slip) condition is applied on the tube wall. The diameter of the tube and its length are $D = 10\mu m$ and $L_z = 45\mu m$, respectively. The RBC model ($N_v = 500$) is initially placed at the center of the domain.

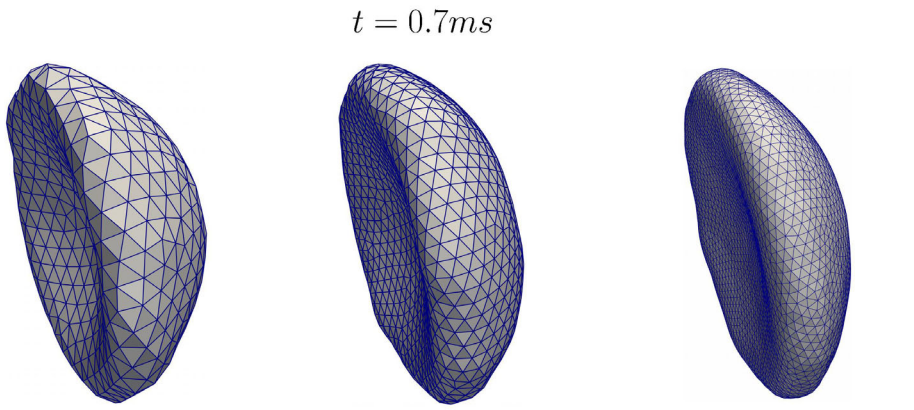

Figure 10. The impact of DPD particles N_v on the membrane dynamics during the fluid-structure interaction simulation. Three values of N_v are examined: a) $N_v = 500$; b) $N_v = 1000$, and c) $N_v = 3000$. The computational setup is shown and discussed in Figure 9, the fluid domain is chosen as Grid-1 (see also Table 2). In all cases, the simulated RBC is compared across different N_v at the time instant $t = 0.7ms$. The RBC is transitioning to the parachute shape. The RBC shape is nearly identical between $N_v = 1000$ and $N_v = 3000$ cases.

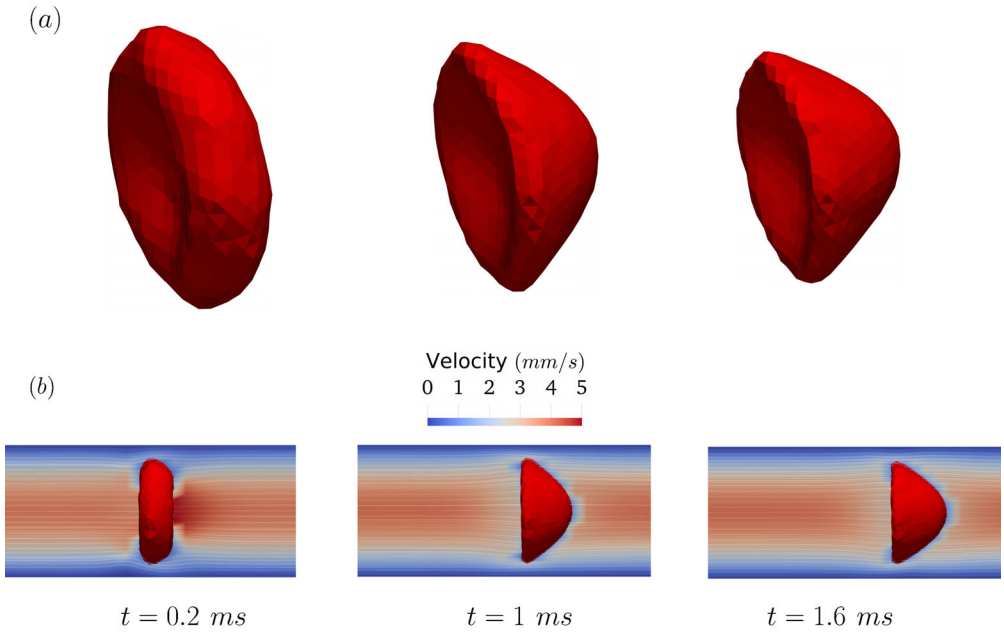

Figure 11. The transition of the RBC shape from the biconcave shape into the parachute shape in Poiseuille flow in Figure 9. The shape of the RBC at $t = 0.2, 1.0$ and 1.6 milliseconds are shown in (a). The corresponding flow field are visualized using velocity contour and in-plane streamlines on one symmetry plane.

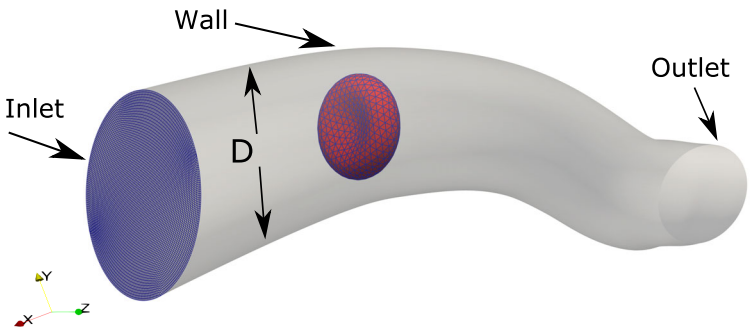

Figure 12. The computational setup for the Fluid-Structure Interaction simulation between a single RBC and the flow in a curved tube, which is a model of human arteriole. a structured grid of size $81 \times 81 \times 141$ with the approximate spacing $0.2\mu m \times 0.17\mu m \times 0.54\mu m$ in the (i, j, k) directions, respectively. The RBC model ($N_v = 500$) is initially placed at a distance of $20\mu m$ from the inlet

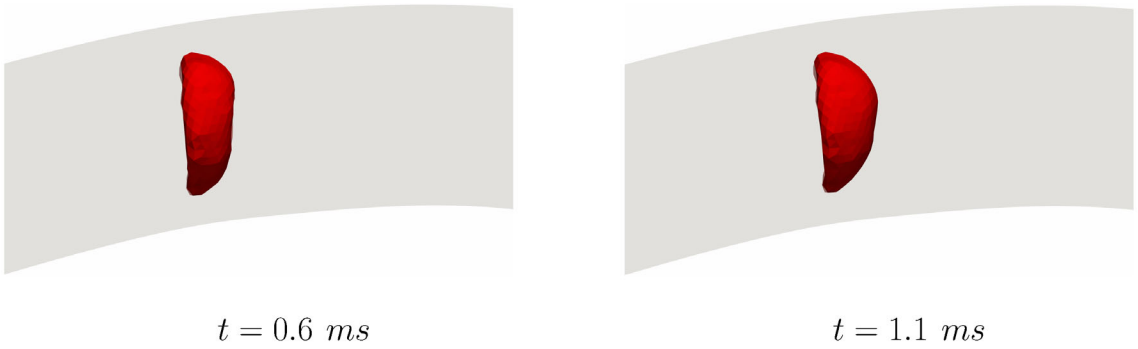

Figure 13. The deformation of the RBC from the biconcave shape into the parachute shape in a curved tube. The shape of the RBC ins show at $t = 0.6$ and 1.1 milliseconds. The tube boundary is shown in the shadow.